



Bioinspired shape shifting of liquid-infused ribbed sheets

Jean Cappello^{a,1} , Benoit Scheid^a, Fabian Brau^b , and Emmanuel Siéfert^{b,1}

Edited by Anna Balazs, University of Pittsburgh, Pittsburgh, PA; received September 19, 2022; accepted November 30, 2022

The recent emergence of stimuli-responsive, shape-shifting materials offers promising applications in fields as different as soft robotics, aeronautics, or biomedical engineering. Targeted shapes or movements are achieved from the advantageous coupling between some stimulus and various materials such as liquid crystalline elastomers, magnetically responsive soft materials, swelling hydrogels, etc. However, despite the large variety of strategies, they are strongly material dependent and do not offer the possibility to choose between reversible and irreversible transformations. Here, we introduce a strategy applicable to a wide range of materials yielding systematically reversible or irreversible shape transformations of soft ribbed sheets with precise control over the local curvature. Our approach—inspired by the spore-releasing mechanism of the fern sporangium—relies on the capillary deformation of an architected elastic sheet impregnated by an evaporating liquid. We develop an analytical model combining sheet geometry, material stiffness, and capillary forces to rationalize the onset of such deformations and develop a geometric procedure to inverse program target shapes requiring fine control over the curvature gradient. We finally demonstrate the potential irreversibility of the transformation by UV-curing a photosensitive evaporating solution and show that the obtained shells exhibit enhanced mechanical stiffness.

shape shifting | hierarchical structure | liquid-infused sheets | inverse program

At a small scale, capillary forces dominate over gravity and may deform elastic structures (1, 2). They can be responsible for catastrophic events, as in the collapse of photoresist lithography structures (3–6), or more dramatically in neonatal lung airway closure (7). However, elastocapillary interactions have also been recently proposed as an efficient route for self-assembly at a small scale, such as for the formation of helical clusters of nanopillars or plates (8–10), four dimensional (4D)-printed curved plates (11), or in the topological transformation of cellular microstructures (12). In all these systems, the slender structures are attached to a thick, nondeformable substrate. Another approach relies on the spontaneous wrapping of a liquid droplet by a thin sheet, producing three dimensional (3D) structures filled with a liquid, in a process that has been named “capillary origami” (13, 14). However, this elegant technique does not provide precise control over the shape of the structure; as the deformation is global, the boundary design appears as the only degree of freedom in the shape selection.

Nature offers an alternative strategy, that capitalizes on the use of a hierarchical structure. The fern sporangium consists in an annulus of cells enclosing the plant spores (15) that opens and ejects them through an elastocapillary mechanism (16). When water evaporates from the cells, the capillary forces apply a torque on the cell walls, leading to the opening of the annulus and, as evaporation continues, cavitation eventually occurs, catapulting the spores. Inspired by this idea, we study the elastocapillary deformation of soft liquid-infused textured sheets, as the liquid evaporates (see Fig. 1*A*, *Materials and Methods*, *Elastomer Preparation*, *Experimental Apparatus*, and *SI Appendix*, Fig. S1). This system is similar to slippery liquid-infused textured surfaces, known for their reduced friction and stable oleophobicity and hydrophobicity (17–19), with the crucial differences being that here the textures and the substrate are soft and that the infusing liquid evaporates. Depending on the stiffness of the material, the geometry of the structured sheet, and the surface tension of the liquid, three scenarios, that we aim at rationalizing, may be observed (Fig. 1*A* and *Movie S1*): i) the sheet remains undeformed, ii) curls (Fig. 1*B*), or iii) has its textures collapse (Fig. 1*C*).

In the limit of a thick sheet, i.e., when the deformation of the sheet is negligible, the system is equivalent to the deformation of soft walls on stiff substrates (Fig. 2*A*), that has been extensively studied in the literature (20–25). Initially, the air–liquid interface between consecutive walls is pinned at the two walls’ corners. As the liquid evaporates, the curvature of the interface increases, and the pressure within the liquid decreases. This process induces a torque per unit distance scaling as $\gamma h^2/d$, with γ the surface tension of the liquid, h the height of the walls, and d the distance between two neighboring

Significance

Plants offer plenty of inspiring examples of deformable hierarchical structures. One of them is the fern sporangium that uses the capillary pressure at the scale of the cells to unbend the whole structure and release the spores. Here, we mimic this deformation mechanism by impregnating soft textured sheets that curl when the liquid evaporates. We derive an analytical model to predict under which conditions such curling occurs. We additionally show that the shape of the deformed structure can be easily inverse-programmed since its final curvature is directly related to the local textures’ geometry. Thus, our study presents a strategy and offers a rational design for the manufacturing of passive self-folding structures at a scale smaller than the capillary length.

Author affiliations: ^aTransfers, Interfaces and Processes, Université libre de Bruxelles, 1050 Brussels, Belgium; and ^bNonlinear Physical Chemistry Unit, Université libre de Bruxelles, 1050 Brussels, Belgium

Author contributions: J.C. and E.S. designed research; J.C. and E.S. performed research; J.C. and E.S. analyzed data; and J.C., B.S., F.B., and E.S. wrote the paper.

The authors have no competing interest.

This article is a PNAS Direct Submission.

Copyright © 2022 the Author(s). Published by PNAS. This article is distributed under [Creative Commons Attribution-NonCommercial-NoDerivatives License 4.0 \(CC BY-NC-ND\)](https://creativecommons.org/licenses/by-nc-nd/4.0/).

¹To whom correspondence may be addressed. Email: jean.cappello@ulb.be or emmanuel.siefert@ulb.be.

This article contains supporting information online at <http://www.pnas.org/lookup/suppl/doi:10.1073/pnas.2216001120/-DCSupplemental>.

Published December 29, 2022.

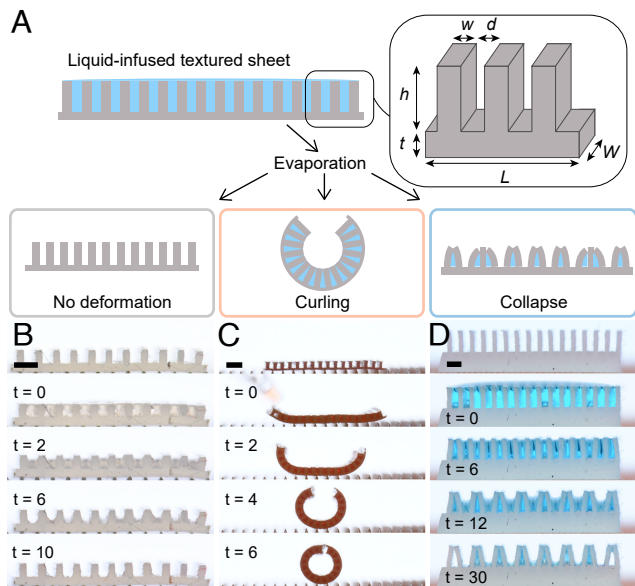


Fig. 1. Deformation scenarios for a soft liquid-infused ribbed sheet. (A) Depending on its stiffness and geometry, the ribbed sheet may either curl, have the structures collapse, or remain undeformed as the liquid evaporates. Snapshots of the three configurations: no deformation (B), curling into a tube (C), and collapse of the walls (D) of impregnated ribbed sheets, as the impregnating liquid (ethanol) evaporates. Scale bars, 1 mm; time is given in minutes.

walls (Fig. 1A). In order to collapse into contact, the walls should deflect by a typical distance d , yielding a bending restoring torque $B_w d/h^2$, where $B_w = Ew^3/[12(1-\nu^2)]$ is the wall bending stiffness with w the wall thickness and ν the Poisson ratio. Balancing both moments, we get the criterion for wall collapse $\gamma h^4/(B_w d^2) > 1/2$ (23). A more detailed model, presented in *SI Appendix, Model for Collapse*, yields the prefactor of the aforementioned scaling criterion. In an array of walls, however, the capillary aggregation is the result of a symmetry-breaking phenomenon as liquid is present on both sides of the walls, but it does not alter the coalescence criterion (23, 24).

In the case of sheet curling, the walls, by symmetry, remain undeformed and may thus be considered rigid (Fig. 2B). Capillary forces induce, via the rigid walls, a torque on the sheet, which still scales as $\gamma h^2/d$. Contact between the top of two neighboring walls occurs for a typical curvature of the sheet of h^{-1} , corresponding to a bending moment B_s/h , where $B_s = Et^3/[12(1-\nu^2)]$ is the sheet bending stiffness. Balancing both torques, we get the criterion for sheet curling $\gamma h^3/(B_s d) > 1/4$. *Movie S2* illustrates the two dynamics occurring below and above the curling threshold. A more detailed model derived in *SI Appendix, Model for Curling* yields the prefactor. It is based on a linear beam model coupled with capillary forces for a varying liquid volume AW and enables us to investigate the evolution of the walls' edge distance Δ as a function of A (Fig. 2C and *SI Appendix, Fig. S3*). When $\gamma h^3/(B_s d) < 1/4$, the structure slightly deforms as A decreases and Δ decreases to reach a minimum before it increases when the contact line detaches from the top edge of the walls, leading to a reopening of the structure (Fig. 2C, *Top*). In contrast, when $\gamma h^3/(B_s d) > 1/4$, Δ decreases monotonically with decreasing A until contact between the two walls occurs (Fig. 2C, *Bottom*). The configurations highlighted by two dashed lines in Fig. 2C correspond to a reopening and a closure of the structure in the vicinity of the transition and

are displayed on the *Top* and *Bottom* of Fig. 2C. In this model, both the adhesion of the sheet on the substrate and the weight of the wet structures have been neglected. In the experiments, the sheets are indeed placed on a rigid plate covered with regularly spaced cones to drastically reduce the area of contact and hence the adhesion (*SI Appendix, Fig. S1*). The wet structures are also sufficiently small, with a length typically of the order of the capillary length, to ensure that capillary forces dominate over gravity (*SI Appendix, Competition Between Capillary Force and Gravity* for more details). The dynamics of sheet curling is governed by the liquid evaporation rate at the air–liquid interfaces, with a typical curling timescale proportional to the height of the textures (*SI Appendix, Comments on the Dynamics*). Hence, the smaller the structure, the faster the curling.

Fig. 2D presents a state diagram rationalizing the regions of the parameter space where sheet curling, wall collapse, or absence of coalescence—shown in orange, blue, and gray, respectively—occurs, showing excellent agreement between the models and the experiments. Note that, in the regime where both curling and collapse are energetically favorable, curling is observed since it leads to the suppression of all the air–liquid interfaces between the walls, whereas in the case of collapse, liquid–air interfaces remain between adjacent collapsed assemblies.

Having derived under which conditions a planar textured sheet curls, we now seek to program its resulting 2D shape and then extend our strategy to the manufacturing of 3D shells. In the curling regime, the edges of neighboring walls get in contact and their geometry sets the coarse-grained radius of curvature of the outer part of the structure R_{th} (Fig. 3A). Neglecting the thickness of the sheet, two consecutive walls are rotated by an angle $\Delta\theta \simeq d/h$ along an arclength $\Delta s = (w + d)$. Thus, we get $R_{th} = \Delta s/\Delta\theta \simeq h(1 + w/d)$. Taking into account the sheet thickness t , a similar geometric reasoning yields the following more precise formula (details are given in *SI Appendix, Programming the Curvature*):

$$R_{th} = h \left(1 + \frac{w}{d} \right) + t \left(1 + \frac{w}{2d} \right). \quad [1]$$

As shown in Fig. 3B, this simple geometric relationship accurately predicts the radius of curvature R_{exp} measured on the curling structures used to construct the state diagram (Fig. 2D). The local radius of curvature depending solely on the geometry of two consecutive ribs (when $t \ll h$), our system offers a unique and easy opportunity to control the local curvature over the structure by varying the height, the width, or the space between the ribs or any combinations of these three quantities. An example of the programming of a heart structure with piecewise constant curvature is shown in Fig. 3C and in *Movie S3*. Fixing the quantities $w + d$ and h/d , we compute the necessary geometry of the ribs such that the sheet curls into the target shape (*SI Appendix, Programming the Curvature* for details on the inverse program). The fabricated flat ribbed sheet is then impregnated with ethanol and curls into the target shape as the liquid evaporates. Following the same strategy, the inverse program may be used to design more complex structures with continuous gradients of curvature such as the Archimedean spiral shown in Fig. 3D (*SI Appendix, Fig. S5*). The target curve (shown at the *Center*) is obtained by varying either the width w (*Top*) or the height h (*Bottom*) of the walls. Computed initial and final shapes (blue panel) are compared to elastocapillary experiments (red panel and *Movie S4*) showing very satisfactory results for both strategies.

This geometric strategy—consisting in using self-contact between simple textures to accurately program the final curvature—

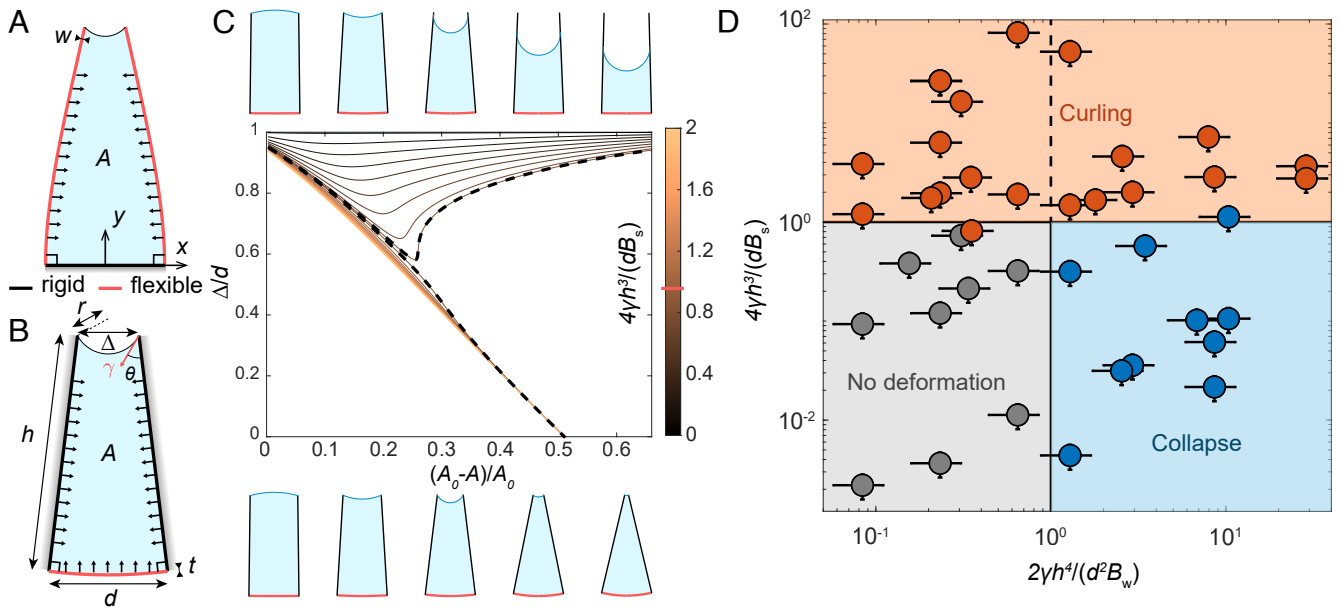


Fig. 2. Rationalization of the deformation modes. (A) Schematic of the model for collapse: two flexible walls, connected by a rigid sheet, deform as the volume AW of liquid reduces, inducing a capillary suction and thus a load along the two walls. (B) Schematic of the model for curling: the walls are considered rigid and the sheet flexible. (C) Rescaled distance Δ/d between the top of the walls as a function of the volume variation as the curling elastocapillary number is varied. Dashed lines correspond to two scenarios close to the transition between curling to contact or reopening (highlighted in red on the color bar); schematics of the corresponding configurations are given on the bottom and on the top, respectively. (D) State diagram rationalizing the regions of the parametric space where no deformation (gray), wall collapse (blue), or sheet curling (orange) occurs. Circles correspond to experiments with $400 \leq h \leq 2,000$, $60 \leq t \leq 1,700$, $200 \leq w \leq 400$, $175 \leq d \leq 500 \mu\text{m}$, $E = 90 \text{ kPa}$, and $\gamma = 22 \text{ mN/m}$.

is general and may be applied to other experimental systems (26). We thus 3D printed the same structures at the centimeter scale and insert a Nylon thread that passes through small holes in the walls, that we attach at one extremity (see *Materials and Methods, Fabrication of Tendon-Based Actuated Structures*, and *SI Appendix, Fig. S2*). As tension is applied to the thread-free extremity, a

torque is induced, leading to the bending of the sheet until the walls come into contact (Fig. 3D, gray region and *Movie S4*). This procedure mimics the tensile mechanism of capillary force at a larger scale and is referred to as the tendon-based actuation.

Although unidirectional curling may be easily programmed, bending simultaneously a planar sheet along two directions

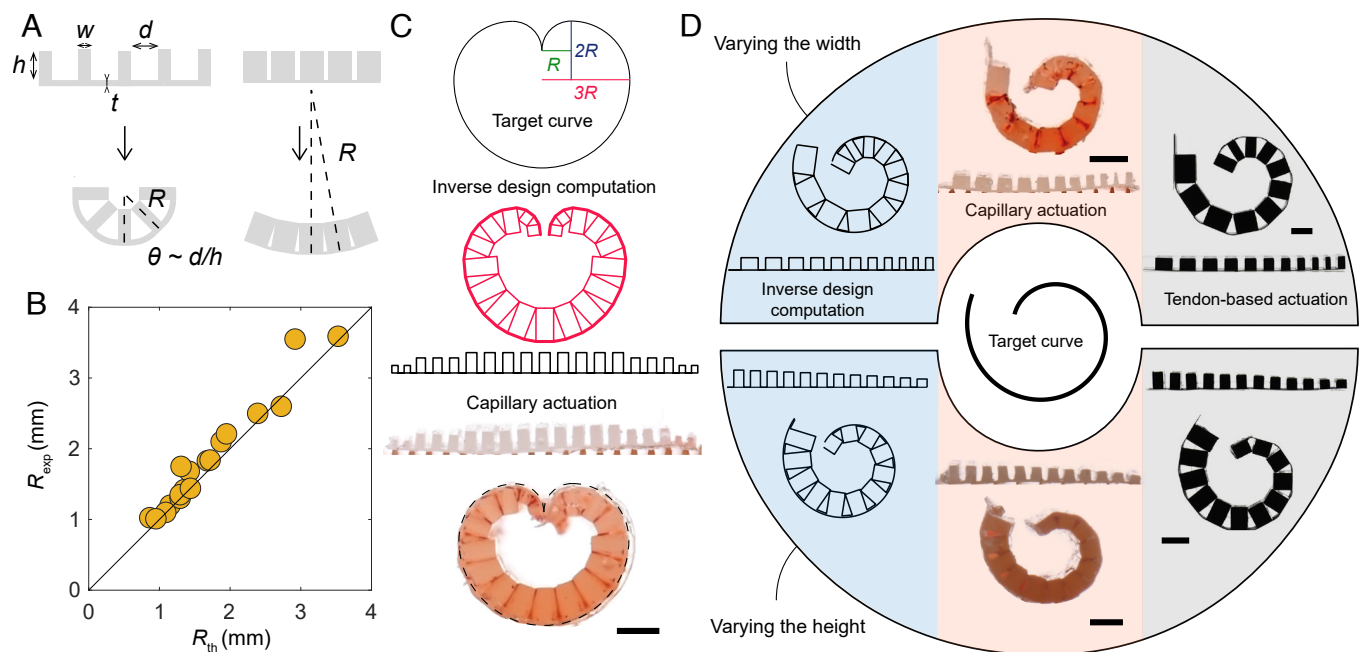


Fig. 3. Programming the curvature. (A) Schematic showing the influence of the texture geometry on the resulting radius of curvature R . (B) Experimental vs. theoretical (Eq. 1) radii of curvature for curling structures. (C) Inverse programming a heart shape, with piecewise constant curvature. (D) Inverse programming of an Archimedean spiral using a gradient in wall width (Top) or height (Bottom). Two experimental strategies are presented: capillary-induced (orange) and tendon-based (black) actuation. Scale bars, 1 mm for capillary-actuated and 1 cm for tendon-actuated structures.

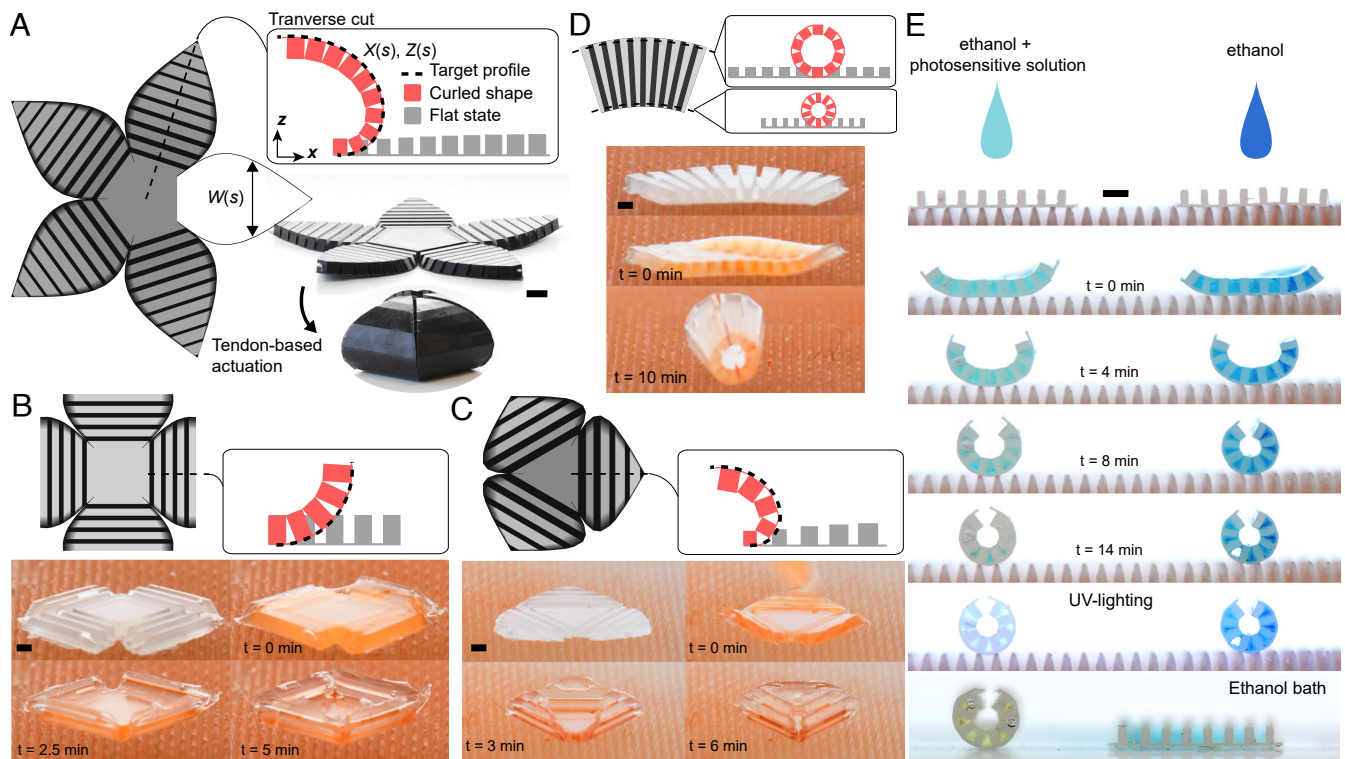


Fig. 4. From architected capillary origami to self-shaping solids. (A) Inverse programming of a closing shell with five facets; the textured geometry is computed from the target profile of the shell using the same methods as in Fig. 3, keeping here the period $w + d$ and the aspect ratio h/w constant. The width W and the bevel of the are then deduced using Eq. 2 together with Eq. 42 of *SI Appendix*, respectively. (B) Self-shaping bowl with four facets and (C) closed shell with three facets actuated by capillary forces. (D) Varying linearly the width w of the walls, cones may also be programmed. (E) Fixing the 3D shape. Two different infusing liquids are used; a photosensitive solution (ethanol, PEG-DA, and photoinitiator at 75%, 24%, and 1% in weight) (Left) and pure ethanol (Right). The curled structures are exposed to UV light and then put in a liquid tank leading to a reopening of the uncured sample, whereas the cured one remains in shape. Scale bars, 1 mm for capillary-actuated and 1 cm for tendon-actuated structures.

yields a new surface which is not locally isometric to the initial state, as demonstrated by Gauss in the Theorema Egregium. Overcoming this limitation necessarily requires large in-plane sheet strains (27), such as in the case of liquid crystal (28, 29), pneumatic (30–32) or dielectric elastomers (33), shape-memory materials (34, 35) or swelling hydrogels (36–39). Such large strains are not to be expected with our ribbed sheet geometries and the capillary forces at play. The proposed strategy can nonetheless be extended to 3D shells by designing structures with judicious boundary design (Fig. 4 A–C), allowing for sheet curling along various directions. Fig. 4A and *Movie S5* show a tendon-based flower composed of five petals, that transforms under radial actuation into a completely closed hollow shell. The geometries of the ribs (gray scheme in the framed panel) are derived using the inverse program in order to match the target profile of parametric coordinates $(X(s), Z(s))$, with s the curvilinear abscissa, of each petal (dashed curve in the framed panel), imposing here constant w/h and $w + d$. The boundary shape of the petals is then deduced by the geometric relation

$$W(s) = 2X(s) \tan[\pi/n], \quad [2]$$

where n is the number of petals (40). Note that, in order to have a complete closure of the flower taking into account its thickness, the edges of the petals are beveled with an angle that depends on the local orientation of each rib in the deformed state (see *SI Appendix Inverse Programming of Self Folding Shells* for further details).

This inverse programming strategy can be used at a smaller scale to make capillary origami structures, that may self-assemble

to any desired faceted target shape, such as a 4-faces bowl or a 3-faces closed shell with an Archimedean spiral profile (Fig. 4 B and C and *Movie S6*). The number of petals may be easily adapted using Eq. 2. Note however that, when the petal width W is of the same order as h , the meniscus becomes fully 3D, leading to a reduced capillary suction preventing the closure of the structure. Other developable shapes, such as a cone (Fig. 4D and *Movie S6*), can also be programmed by radially varying the wall width w , while keeping the local rotation angle d/h constant.

To conclude, we presented in this article a simple yet general elastocapillary system that takes advantage of the textures on a planar elastic sheet to precisely program 3D shapes as an impregnating liquid evaporates. It may be applied to many liquid/solid pair, given that the liquid sufficiently wets the sheet, and we provide a rationale to design the geometry of the textured sheet such that it may curl. While the sheets were infused in this study by depositing a drop, the structure may also be dip-coated (41), leading to the same shape changes (*Movie S7*). Once actuated, the idea of using self-contact between adjacent textures to program the curvature is purely geometric and thus scale-free and may be adapted to other actuation mechanisms, such as tendon-based or vacuum actuators (42). This reversible mechanism can be easily turned into an irreversible shape transformation (Fig. 4E and *Movie S8*). The evaporating liquid can indeed be mixed with a photosensitive solution that cures when exposed to UV light, leading to an elastic composite structure with a fixed shape (see *Materials and Methods*, and *Preparation of Photosensitive Infusing Liquid* for details). Most importantly, this method enables the reliable manufacturing of closed empty—and not fluid-filled—shells, which is not possible

with standard capillary origami or laser lithography 3D printing techniques. Moreover, as neighboring walls and petals come in contact, such shells transition from a sheet bending deformation mode to a stretching one, exhibiting thus a dramatic increase in stiffness and resistance to poking (*SI Appendix, Fig. S7 and Movie S9*) (43). The liquid may also be absorbed by the ribbed sheets and lead to swelling (12, 44), opening alternative routes to enrich the space of reachable shapes. We believe that these concepts will open the way to capabilities in the microfabrication and nanofabrication of 3D structures, with innovative applications in view, for the mass production of microrobot swarms (45), or the design of biomedical devices and targeted drug delivery systems (46).

Materials and Methods

Elastomer Preparation. The structures are made of polyvinyl siloxane rubber (Smooth-On 00-50 or 00-35 fast) and are fabricated by mixing a prepolymer base and a curing catalyst in a 1:1 weight ratio. Just after mixing, when the melt is still liquid, it is poured on a 3D-printed mold and spin-coated (SCS 6,800 SpinCoater Series) at various rotation speeds that control the sheet thickness. Alternatively, in the case of large gradients in the textures' geometry, a flat cover with spacers is carefully placed on the mold to set the sheet thickness. The polymer melt gradually cures over time, leading to an elastic solid. At room temperature, the curing time is 2 h (Smooth-On 00-50) or 10 min (Smooth-On 00-50 fast). The design of the molds is realized using MATLAB and OpenSCAD and the print with either a Prusa SL1 or a Ultimaker S5. Prints made with Prusa SL1 are cleaned and postcured in a UV chamber overnight to ensure proper curing of the silicon rubber.

Experimental Apparatus. Schematics of our experiments are shown in *SI Appendix, Fig. S1*. The structured sheets are placed on top of an array of cones (the microcones array being printed with the Prusa SL1 3D printer). By this mean adhesion between the structured sheet and the substrate on top of which it sits is dramatically reduced. Droplets of wetting liquid (ethanol or the photosensitive solution) are then deposited on the sheet and impregnate all the ribs of the structure. Then, while evaporation occurs, the deformation of the structure is recorded using a camera (Nikon D850), and the curvature is extracted from images by standard image processing using ImageJ (47). When

a photosensitive solution is used as the infusing liquid, once the structure has reached its final and desired shape it is enlightened with a UV source, leading to the cross-link of the photosensitive solution which forms a hydrogel. The wavelength emitted by the source needs to match the excitation wavelength of the photoinitiator in order to get cross-linking. Once the hydrogel is formed, the composite object composed of the silicon rubber structure and the cross-linked hydrogel behaves as an elastic object. Cross-linking of the oligomer solution is accompanied by a small shrinkage of the hydrogel at the origin of prestress in the assembled structure. Changing the nature of the oligomer can help decrease/increase this prestress depending on the effects sought.

Preparation of Photosensitive Infusing Liquid. The photosensitive solution is composed of a solvent (ethanol, Sigma-Aldrich) at 75% in weight, an oligomer (PEG-DA $M_n = 700$ g/mol, Sigma-Aldrich), at 24% in weight, and a photoinitiator of excitation wavelength $\lambda = 390$ nm diphenyl(2,4,6-trimethylbenzoyl)phosphine oxide (TPO), Sigma-Aldrich, at 1% in weight. To ease its manipulation, the PEG-DA $M_n = 700$ g/mol, which is solid at ambient temperature, is melted at 50° . Mixing of all the components is achieved with a vortex mixer.

Fabrication of Tendon-Based Actuated Structures. Tension-based actuated structures are fabricated following two steps. First, the structured elastic sheet is 3D-printed with an Ultimaker S5 FDM printer using Ultimaker Tough PLA (polylactic acid) material. Second, the ribs are designed with a cylindrical hole at their center such that a Nylon thread may be inserted. The thread is attached to one end of the structure while the other end is free and may be pulled to actuate the tendon-based mechanism. Sketches and pictures of a tension-based actuated structure are shown in *SI Appendix, Fig. S2*.

Data, Materials, and Software Availability. All study data are included in the article and/or *SI Appendix*.

ACKNOWLEDGMENTS. We acknowledge support by F.R.S.-FNRS under the research grants no. T.0025.19 (PDR "ElastoCap") and no. J.0017.21 (CDR "FASTER"). This project has received funding from the European Union's Horizon 2020 research and innovation program under the Marie Skłodowska-Curie grant agreement no. 101027862 and funding from 747 Fédération Wallonie-Bruxelles (ARC ESCAPE project).

1. B. Roman, J. Bico, Elasto-capillarity: Deforming an elastic structure with a liquid droplet. *J. Phys.: Condens. Matter* **22**, 493101 (2010).
2. J. Bico, É. Reyssat, B. Roman, Elastocapillarity: When surface tension deforms elastic solids. *Annu. Rev. Fluid Mech.* **50**, 629–659 (2018).
3. T. Tanaka, M. Morigami, N. Atoda, Mechanism of resist pattern collapse during development process. *Jpn. J. Appl. Phys.* **32**, 6059 (1993).
4. N. Chakrapani, B. Wei, A. Carrillo, P. M. Ajayan, R. S. Kane, Capillarity-driven assembly of two-dimensional cellular carbon nanotube foams. *Proc. Natl. Acad. Sci. U.S.A.* **101**, 4009–4012 (2004).
5. O. Raccurt, F. Tardif, F. A. d'Avitaya, T. Vareine, Influence of liquid surface tension on stiction of SOI MEMS. *J. Micromech. Microeng.* **14**, 1083 (2004).
6. J. H. Jang *et al.*, 3D micro- and nanostructures via interference lithography. *Adv. Funct. Mater.* **17**, 3027–3041 (2007).
7. M. Heil, A. L. Hazel, J. A. Smith, The mechanics of airway closure. *Res. Physiol. Neurobiol.* **163**, 214–221 (2008).
8. M. Mastrangeli *et al.*, Self-assembly from milli- to nanoscales: Methods and applications. *J. Micromech. Microeng.* **19**, 083001 (2009).
9. B. Pokroy, S. H. Kang, L. Mahadevan, J. Aizenberg, Self-organization of a mesoscale bristle into ordered, hierarchical helical assemblies. *Science* **323**, 237–240 (2009).
10. M. De Volder, A. J. Hart, Engineering hierarchical nanostructures by elastocapillary self-assembly. *Angew. Chem. Int. Ed.* **52**, 2412–2425 (2013).
11. X. Liu *et al.*, Capillary-force-driven self-assembly of 4D-printed microstructures. *Adv. Mater.* **33**, 2100332 (2021).
12. S. Li *et al.*, Liquid-induced topological transformations of cellular microstructures. *Nature* **592**, 386–391 (2021).
13. C. Py *et al.*, Capillary origami: Spontaneous wrapping of a droplet with an elastic sheet. *Phys. Rev. Lett.* **98**, 156103 (2007).
14. J. Paulsen *et al.*, Optimal wrapping of liquid droplets with ultrathin sheets. *Nat. Mat.* **14**, 1206 (2015).
15. X. Noblin *et al.*, The fern sporangium: A unique catapult. *Science* **335**, 1322 (2012).
16. R. T. Borno, J. D. Steinmeyer, M. M. Maharbiz, Transpiration actuation: The design, fabrication and characterization of biomimetic microactuators driven by the surface tension of water. *J. Micromech. Microeng.* **16**, 2375 (2006).
17. T. S. Wong *et al.*, Bioinspired self-repairing slippery surfaces with pressure-stable omniphobicity. *Nature* **477**, 443–447 (2011).
18. J. D. Smith *et al.*, Droplet mobility on lubricant-impregnated surfaces. *Soft Matter* **9**, 1772–1780 (2013).
19. A. Keiser, L. Keiser, C. Clanet, D. Quéré, Drop friction on liquid-infused materials. *Soft Matter* **13**, 6981–6987 (2017).
20. M. Taroni, D. Vella, Multiple equilibria in a simple elastocapillary system. *J. Fluid Mech.* **712**, 273–294 (2012).
21. K. Singh, J. R. Lister, D. Vella, A fluid-mechanical model of elastocapillary coalescence. *J. Fluid Mech.* **745**, 621–646 (2014).
22. Z. Wei *et al.*, Elastocapillary coalescence of plates and pillars. *Proc. R. Soc. A* **471**, 20140593 (2015).
23. T. H. Kim, J. Kim, H. Y. Kim, Evaporation-driven clustering of microscale pillars and lamellae. *Phys. Fluids* **28**, 022003 (2016).
24. A. Hadjittofis, J. R. Lister, K. Singh, D. Vella, Evaporation effects in elastocapillary aggregation. *J. Fluid Mech.* **792**, 168–185 (2016).
25. A. T. Bradley, I. J. Hewitt, D. Vella, Bendocapillary instability of liquid in a flexible-walled channel. *arXiv [preprint]* (2022). <http://arxiv.org/abs/2201.01103>.
26. R. Guseinov, E. Miguel, B. Bickel, Curveups: Shaping objects from flat plates with tension-actuated curvature. *ACM Trans. Graphics (TOG)* **36**, 1–12 (2017).
27. E. Efrati, E. Sharon, R. Kupferman, Buckling transition and boundary layer in non-Euclidean plates. *Phys. Rev. E* **80**, 016602 (2009).
28. T. J. White, D. J. Broer, Programmable and adaptive mechanics with liquid crystal polymer networks and elastomers. *Nat. Mat.* **14**, 1087–1098 (2015).
29. H. Aharoni, Y. Xia, X. Zhang, R. D. Kamien, S. Yang, Universal inverse design of surfaces with thin nematic elastomer sheets. *Proc. Natl. Acad. Sci. U.S.A.* **115**, 7206–7211 (2018).
30. R. F. Shepherd *et al.*, Multigait soft robot. *Proc. Natl. Acad. Sci. U.S.A.* **108**, 20400–20403 (2011).
31. E. Siéfert, E. Reyssat, J. Bico, B. Roman, Bio-inspired pneumatic shape-morphing elastomers. *Nat. Mat.* **18**, 24–28 (2019).
32. T. J. Jones, E. Jambon-Puillet, J. Marthelot, P. T. Brun, Bubble casting soft robotics. *Nature* **599**, 229–233 (2021).

33. E. Hajiesmaili, D. R. Clarke, Reconfigurable shape-morphing dielectric elastomers using spatially varying electric fields. *Nat. Commun.* **10**, 183 (2019).
34. N. Choudhary, D. Kaur, Shape memory alloy thin films and heterostructures for mems applications: A review. *Sens. Actuators A: Phys.* **242**, 162–181 (2016).
35. H. Meng, G. Li, A review of stimuli-responsive shape memory polymer composites. *Polymer* **54**, 2199–2221 (2013).
36. Y. Klein, E. Efrati, E. Sharon, Shaping of elastic sheets by prescription of non-Euclidean metrics. *Science* **315** (2007).
37. J. Kim, J. A. Hanna, M. Byun, C. D. Santangelo, R. C. Hayward, Designing responsive buckled surfaces by halftone gel lithography. *Science* **335**, 1201–1205 (2012).
38. A. S. Gladman, E. A. Matsumoto, R. G. Nuzzo, L. Mahadevan, J. A. Lewis, Biomimetic 4D printing. *Nat. Mat.* **15** (2016).
39. L. Huang *et al.*, Ultrafast digital printing toward 4D shape changing materials. *Adv. Mat.* **29**, 1605390 (2017).
40. M. Liu, L. Domino, D. Vella, Tapered elasticæ as a route for axisymmetric morphing structures. *Soft Matter* **16**, 7739–7750 (2020).
41. P. M. Reis, J. Hure, S. Jung, J. W. Bush, C. Clanet, Grabbing water. *Soft Matter* **6**, 5705–5708 (2010).
42. S. Li, D. M. Vogt, D. Rus, R. J. Wood, Fluid-driven origami-inspired artificial muscles. *Proc. Natl. Acad. Sci. U.S.A.* **114**, 13132–13137 (2017).
43. Y. Wang, L. Li, D. Hofmann, J. E. Andrade, C. Daraio, Structured fabrics with tunable mechanical properties. *Nature* **596**, 238–243 (2021).
44. Y. Tao *et al.*, Morphing pasta and beyond. *Sci. Adv.* **7**, eabf4098 (2021).
45. M. Z. Miskin *et al.*, Electronically integrated, mass-manufactured, microscopic robots. *Nature* **584**, 557–561 (2020).
46. M. Sitti, Miniature soft robots-road to the clinic. *Nat. Rev. Mat.* **3**, 74 (2018).
47. C. A. Schneider, W. S. Rasband, K. W. Eliceiri, NIH image to imageJ: 25 years of image analysis. *Nat. Methods* **9**, 671–675 (2012).